CHEMISTRY OF MATERIALS

pubs.acs.org/cm Article

X-ray Spectroscopy of (Ba,Sr,La)(Fe,Zn,Y)$O_{3-\delta}$ Identifies Structural and Electronic Features Favoring Proton Uptake

Giulia Raimondi, Francesco Giannici,* Alessandro Longo,* Rotraut Merkle,* Alessandro Chiara, Maximilian F. Hoedl, Antonino Martorana, and Joachim Maier

Cite This: *Chem. Mater.* 2020, 32, 8502–8511 Read Online

ACCESS | Metrics & More | Article Recommendations | Supporting Information

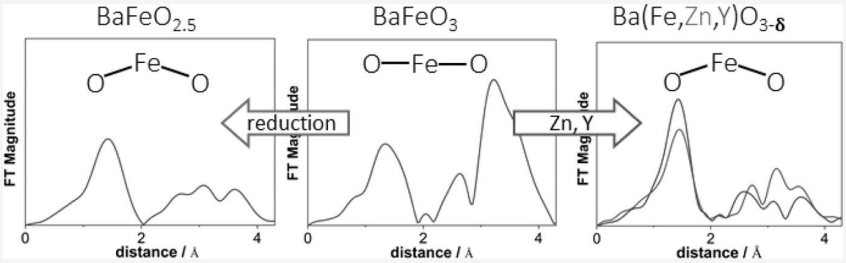

ABSTRACT: Mixed protonic–electronic conducting oxides are key functional materials for protonic ceramic fuel cells. Here, (Ba,Sr,La)(Fe,Zn,Y)$O_{3-\delta}$ perovskites are comprehensively investigated by X-ray spectroscopy (in oxidized and reduced states). Extended X-ray absorption fine structure shows that Zn,Y doping strongly increases the tendency for Fe–O–Fe buckling. X-ray absorption near-edge spectroscopy at the Fe K-edge and X-ray Raman scattering at the O K edge demonstrate that both iron and oxygen states are involved when the samples are oxidized, and for the Zn,Y doped materials, the hole transfer from iron to oxygen is less pronounced. This can be correlated with the observation that these materials show the highest proton uptake.

1. INTRODUCTION

Protonic ceramic fuel cells (PCFC) have the potential to bridge the gap between conventional solid oxide fuel cells based on oxygen-ion conducting electrolytes operating typically at ≥ 700 °C and polymer-based fuel cells operating near room temperature. Proton-conducting ceramic electrolytes attain the required ionic conductivities of 0.1 S/cm, a value that even exceeds for Ba(Zr,Ce,Y)$O_{3-\delta}$ above 400 °C.[1] A further advantage besides a favorable compromise between stability and kinetics is that water is produced mainly at the cathode side, which facilitates operation at high fuel utilization. On the lab scale, PCFCs have made significant progress in recent years, which resulted from the combination of optimized electrolyte composition and processing, as well as specifically adjusted cathode material compositions (see e.g.,[2−6]). To allow the oxygen reduction to water to proceed on the whole cathode surface, the cathode material requires a proton conductivity in the range of 10^{-5} to 10^{-4} S/cm.[7] PCFC cathodes are typically perovskites (e.g., refs[2,3,5]) or perovskite-related materials (e.g., double perovskites[4,8] or Ruddlesden–Popper phases[9]). They show p-type electronic conductivity and contain oxygen vacancies $V_o^{\bullet\bullet}$ (or empty O interstitial sites) into which water can dissociatively be incorporated, forming protonic defects $OH_o^{\bullet}$ (hydroxide ion on a regular oxygen lattice site; $O_o^{\times}$ is a regular oxide ion)

$$H_2O + V_o^{\bullet\bullet} + O_o^{\times} \leftrightarrow 2OH_o^{\bullet}$$

This is the same reaction that leads to water uptake in electrolytes;[1] however, the degree of hydration (the fraction of available $V_o^{\bullet\bullet}$ filled with $OH_o^{\bullet}$) is significantly lower for cathode perovskites.[10]

Owing to the small proton uptake and the challenges to separate the related compositional changes from oxygen stoichiometry changes, only a limited number of proton uptake measurements of PCFC cathode materials have been made available; see for example, refs 4, 8, and 10–17. The relation of proton uptake to the perovskite cation composition was investigated in the work of Zohourian et al.,[10] which showed that a high Ba content in (Ba,Sr,La)(Fe)$O_{3-\delta}$ perovskites is beneficial for proton uptake. Interestingly, Zn or Y doping on the Fe site significantly increases the proton content (more than expected from the slightly increased concentration of oxygen vacancies $V_o^{\bullet\bullet}$). On the other hand, an increased Fe oxidation state strongly decreases the protonation, as evidenced in experiments[10] and by DFT calculations for (Ba,Sr)$FeO_{3-\delta}$.[18] Both findings must be analyzed in more

Received: June 24, 2020
Revised: September 10, 2020
Published: September 11, 2020

https://dx.doi.org/10.1021/acs.chemmater.0c02655
Chem. Mater. 2020, 32, 8502–8511

detail to further optimize PCFC cathode materials. While extended X-ray absorption fine structure (EXAFS) has been applied for the investigation of proton-conducting perovskite electrolyte materials,[19−22] so far, they are sparse for PCFC cathode materials [the only example is (La,Sr)$MnO_{3\pm\delta}$.[23] To shed light on both the local atomic structure and the electronic structure in (Ba,Sr,La)(Fe,Zn,Y)$O_{3-\delta}$ perovskites, we report here a comprehensive X-ray absorption spectroscopy (XAS) study involving both the B-site cations (Fe,Zn,Y) and the oxygen atoms: this latter absorption edge was investigated with X-ray Raman scattering (XRS). Because the oxygen K-edge lies in the soft X-ray energy range, it is usually measured with surface-sensitive techniques (e.g., total electron yield or Auger effect). With XRS, a high-energy X-ray technique, a large volume of the sample is probed, resulting in an oxygen K-edge spectrum signal, which represents the bulk of the oxide material.[24−29] The combined investigation of transition metals and oxygen edges is particularly important for fuel cell, catalyst, and battery materials which undergo redox processes that possibly affect both elements. Recently, oxygen K-edge XRS has even been applied under in situ conditions during battery cycling[26] and variable temperature.[29]

Here, we investigate (Ba,Sr,La)(Fe,Zn,Y)$O_{3-\delta}$ samples in completely reduced and oxidized states in which iron has a formal valence of 3+ and 4+, respectively. The combination of Fe and O K edge spectra gives a detailed insight how far the change of the Fe oxidation state also affects the properties of the oxide ions in the material. This, in turn, helps to understand the origin of the influence of the Fe oxidation state on the proton uptake, which has been reported in ref 10. (Ba,Sr,La)$FeO_{3-\delta}$ samples with partial B-site substitution by Y^{3+} or Zn^{2+} are investigated to elucidate the specific changes introduced by these oversized dopants, which significantly increase the proton uptake. For several perovskites with redox−active transition metals, a close relation between the buckling of B−O−B configurations and the degree of B−O covalency and charge (de)localization has already been reported.[30−32] Thus, the local structure of the reduced and oxidized (Ba,Sr,La)(Fe,Zn,Y)$O_{3-\delta}$ perovskites is probed by EXAFS. The correlations with the electronic structure from X-ray absorption near-edge spectroscopy (XANES) and XRS, and the trends in measured proton uptake[10] are explored in Section 3.4.

The comprehensive understanding of these complex structural and defect-chemical relations will assist in the further optimization of PCFC cathode materials: these have to find a good compromise between apparently conflicting requirements on electronic conductivity, proton conductivity, catalytic activity for oxygen reduction, and chemical stability.[10]

2. MATERIALS AND METHODS

The list of sample compositions and their abbreviations is given in Table 1. The majority of samples were synthesized from aqueous nitrate solutions, using the citric acid and ethylenediaminetetraacetic acid complexing route,[33] and calcining in air (8 h at 1000 °C). SF was prepared via solid oxide synthesis.[10] An additional high-temperature treatment at 1300 °C was required for BFY20 in order to obtain a phase-pure sample. For BL5F, 5% La doping on the Ba site is necessary to prevent formation of a hexagonal perovskite structure with face-sharing octahedra.[34,35]

Each composition was then treated either by oxidation or by reduction. Oxidation was carried out in an autoclave at 600 bar of pure O_2 from 550 °C, decreasing to 250 °C during 72 h, yielding samples labeled as ox in the following (similar treatment as for $SrTi_{1-x}Fe_xO_{3-\delta}$ in ref 42). The final oxygen stoichiometry of the oxidized samples was checked via thermogravimetry (STA 449 C, Netzsch, Germany) by heating in N_2 to 900 °C or reducing in 1.5% H_2 at 700 °C: both treatments yield a plateau which corresponds to all iron being converted to the 3+ oxidation state (this is typical for iron perovskites; see e.g. refs 36 and 37; see more details in Supporting Information-1). No traces of metallic Fe can be found in X-ray diffraction (XRD) (Figure S1), and there is also no indication for Fe^{2+} or metallic Fe in the XANES and EXAFS spectra. All oxidized samples were found to reach at least 96% of their nominal O stoichiometry, in line with similar treatments for $SrTi_{1-x}Fe_xO_3$ perovskites.[42] Reduction of samples for XAS was carried out in a tube furnace with 1.5% of H_2 at 700 °C for 4−5 h, yielding samples labeled as red in the following. The oxidized samples have a black color, while the reduced samples are brown (Figure S1 in Supporting Information). All samples have iron in the high-spin state. Sample composition, their final nominal O stoichiometry after the different treatments, formal Fe oxidation states, and lattice parameters are listed in Table 1. Because O interstitials (or cation vacancies) are energetically unfeasible in the perovskite structure, the formal iron oxidation state remains below 4+ in BL5Fox and BL25Fox. Moreover, because formal Fe^{5+} is also unfavorable, oxidized Y,Zn-doped samples contain 0.1−0.2 oxygen vacancies per formula unit. For better readability, we refer to the sample containing 20% of zinc or yttrium in the B-site simply as doped samples.

Table 1. Notation, Stoichiometry, Formal Fe Oxidation State, and Lattice Parameters for All Samples after the Reduction/Oxidation Treatment[a]

sample	stoichiometry	formal Fe oxidation state	lattice parameters/Å
SFox	$SrFeO_{3.00}$	4+	3.85
SFred	$SrFeO_{2.50}$	3+	5.52, 5.67, 15.60,[10] pseudocubic: 3.94
BL25Fox	$Ba_{0.75}La_{0.25}FeO_{3.00}$	3.875*	3.95
BL25Fred	$Ba_{0.75}La_{0.25}FeO_{2.625}$	3+	4.02
BL5Fox	$Ba_{0.95}La_{0.05}FeO_{3.00}$	3.975*	3.99
BL5Fred	$Ba_{0.95}La_{0.05}FeO_{2.525}$	3+	4.08
BL5FZn20ox	$Ba_{0.95}La_{0.05}Fe_{0.8}Zn_{0.2}O_{2.825}$	4+	4.06
BL5FZn20red	$Ba_{0.95}La_{0.05}Fe_{0.8}Zn_{0.2}O_{2.425}$	3+	4.08
BFY20ox	$BaFe_{0.8}Y_{0.2}O_{2.90}$	4+	4.14
BFY20red	$BaFe_{0.8}Y_{0.2}O_{2.50}$	3+	4.14
BSFox	$Ba_{0.5}Sr_{0.5}FeO_{3.00}$	4+	3.92
BSFred	$Ba_{0.5}Sr_{0.5}FeO_{2.50}$	3+	4.00
BSFZn20ox	$Ba_{0.5}Sr_{0.5}Fe_{0.8}Zn_{0.2}O_{2.80}$	4+	3.95
BSFZn20red	$Ba_{0.5}Sr_{0.5}Fe_{0.8}Zn_{0.2}O_{2.40}$	3+	4.01
SFZn20ox	$SrFe_{0.8}Zn_{0.2}O_{2.80}$	4+	3.86
SFZn20red	$SrFe_{0.8}Zn_{0.2}O_{2.40}$	3+	3.91

[a]SFred has an orthorhombic brownmillerite structure. *maximum possible formal oxidation state because O interstitials or cation vacancies are unfeasible.

The cation stoichiometry of the synthesized perovskite powders was checked by inductively coupled plasma optical emission spectroscopy (Spectro Ciros CCD, Spectro Analytical Instruments, Germany). Phase purity of the powders was checked by XRD (Cu Kα, Bragg−Brentano geometry, PANalytical EMPYREAN). All investigated samples have a perovskite cubic structure (space group $Pm\bar{3}m$), with the exception of reduced SF ($Sr_2Fe_2O_5$), which adopts the brownmillerite structure.[10] Rietveld refinement was performed for all samples, and the fitted lattice parameters are included in Table 1.

X-ray absorption measurements were recorded at the BM26 beamline at ESRF (European Synchrotron Radiation Facility, Grenoble, France) using a double-crystal monochromator equipped with Si(111) crystals. The spectra were collected for oxidized and

https://dx.doi.org/10.1021/acs.chemmater.0c02655
Chem. Mater. 2020, 32, 8502−8511

reduced samples, as well as the standards (ZnO, Y_2O_3, and Fe_2O_3). The iron K-edge (7.1 keV), and for the doped samples, zinc (9.7 keV) and yttrium K-edges (17 keV) were measured in transmission mode. For each sample, the powder was mixed with an organic cellulose matrix (microcrystalline cellulose, Sigma-Aldrich) and uniaxially pressed to a pellet. All measurements were acquired at 80 K with a liquid nitrogen cryostat. The k^2-weighted data were extracted with a Bayesian algorithm and fitted using the program Viper;[38] theoretical amplitudes and phases were calculated using the FEFF 9.6.1 code.[39] More details of the EXAFS fitting are given in the Supporting Information.

XRS was performed at the ID20 beamline at ESRF on oxidized and reduced BL5F and BL5FZn20. The sample powders were pressed into a ≈2 mm thick pellet, which was placed at an angle of 7° with the incident beam. The incident beam was monochromatized using a double-crystal Si(111) monochromator and focused to a spot size around 10 × 20 μm^2 with Kirkpatrick-Baez mirrors. The large solid angle spectrometer at ID20 was used to collect XRS data with 36 spherically bent Si(660) analyzer crystals.[40] The overall energy resolution was 1 eV, as estimated from the full width at half maximum of elastic scattering from a piece of adhesive tape. To extract the oxygen K-edge spectra from broader scans (0−900 eV), the data were treated with the XRStools package as described elsewhere,[41] merging data at medium and high momentum transfer (6.2 ± 0.4 $Å^{-1}$). Sample powders were pelletized by cold uniaxial pressing. All measurements were collected at room temperature. Oxygen K-edge spectra in the 520−590 eV range were acquired for 8−10 h per sample, using a 0.2−0.7 eV energy step.

3. RESULTS AND DISCUSSION

3.1. Iron XANES. The Fe K-edge XANES spectrum contains information on the average coordination and oxidation state of iron. In Figure 1 the Fe K-edge XANES

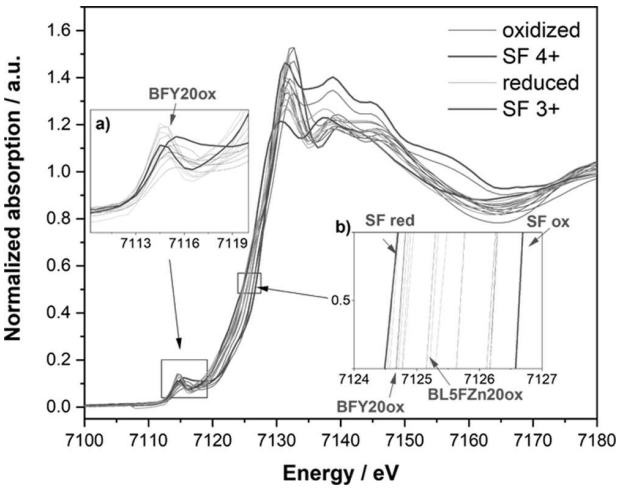

Figure 1. XANES of the iron K-edge of the reduced samples (light green), oxidized samples (red), SFred (olive, bold), and SFox (red, bold). Inset (a) shows the pre-edge region. Inset (b) shows the main absorption edge region.

spectra of all the samples are reported, highlighting oxidized SF ($SrFeO_3$) and reduced SF ($SrFeO_{2.5}$), which are representative of formal Fe^{4+} and Fe^{3+} states (individual plots are shown in Figure S4). In all samples, it is possible to recognize four characteristic features: a pre-edge peak (≈7.115 keV), a narrow white line (≈7.132 keV), and two shallow peaks (≈7.138 and ≈7.145 keV, respectively).

The pre-edge peak is rather sharp for the reduced samples, while for most of the oxidized samples, it is broader and slightly shifts to higher energies (as it is expected from the increased Fe^{4+} content). Interestingly, the pre-edge peak of BFY20ox exhibits almost the same shape and position as BFY20red. As shown in inset (b), the edge position also shifts to higher energies for the oxidized samples. The shift is most pronounced between oxidized and reduced SF, amounting to about 2 eV (the full list of the samples half-height energies is enclosed in Table S1). The trends for pre-edge peak and edge positions are consistent with those observed already in the comparison of reduced and oxidized $Sr(Ti_{1-x}Fe_x)O_{3-\delta}$ perovskites.[42] The edges of BFY20ox (half-height at 7124.6 eV) and BL5FZn20ox (half-height at 7125.2 eV) oxidized samples are located at comparably low energies.

The position of the pre-edge peak and main absorption edge both depend on the effective oxidation state (effective charge) of the transition metal.[42−46] It is also widely accepted that the effective oxidation state of a transition metal cation is significantly lower than its formal oxidation state, in particular, for 4+ cations. The decreased effective oxidation state can be attributed to the partial transfer of electron holes from Fe^{4+} to the adjacent oxygen ions. Such a hole transfer from transition metal to oxygen has also been observed in other iron and cobalt perovskites such as $BaZr_{1-x}Fe_xO_{3-\delta}$ or $Ba_{0.1}Sr_{0.9}Co_{0.8}Fe_{0.2}O_{3-\delta}$.[43,47,48]

The variation in the pre-edge peak and edge positions in Figure 1 demonstrates that the degree of this hole transfer from transition metal to oxygen depends sensitively on the perovskite's cation composition. While all pre-edge peaks and absorption edges for the reduced samples are rather similar, stronger variations can be seen for the oxidized samples. The fact that oxidized SF shows the largest absorption edge shift indicates that iron is closer to Fe^{4+} than in the Ba-rich perovskites. At first glance, this may appear counterintuitive because one might expect a higher degree of covalency for shorter Fe−O bonds. However, covalency is not the only parameter that affects O → Fe charge transfer. The amount of electron transfer from oxygen to iron might be larger in an oxide with higher basicity such as $BaFeO_3$ because of the increased tendency of oxygen to donate electrons. Interestingly, BFY20 and BL5FZn20 show the smallest shift of edge and pre-edge peaks to higher energy upon oxidation (i.e., even in oxidized samples, iron is close to the Fe^{3+} character). This may be related to the fact that partial substitution of Y^{3+},Zn^{2+} on the B site increases the overall basicity of the perovskite (this effect is strongest for the oxidized samples), which in turn allows for more electron transfer from oxygen to iron, decreasing the effective Fe oxidation state. Some more aspects of the hole delocalization, the specific features of Zn- and Y-doped $BaFeO_{3-\delta}$, and its effect on proton uptake will be discussed in Section 3.4. Quantitative modeling of the electronic structure changes, as visible in Fe XANES and O-XRS based on quantum-chemical calculations, will be reported in a forthcoming paper.

3.2. Fe,Y,Zn EXAFS. The EXAFS spectra contain quantitative information about the local atomic arrangements. We fitted the EXAFS spectra up to the third shell (around 4.2 Å) around each of the cations (Fe, Zn, and Y) using a cubic perovskite model. This information is complementary to that gathered by the XRD analysis: in the latter, the average cubic structure is probed, losing the information on the different B−A and B−B distances arising from the different elements residing on the same lattice site. On the local level probed with EXAFS, a mixed occupation of the A and/or B site typically

https://dx.doi.org/10.1021/acs.chemmater.0c02655
Chem. Mater. 2020, 32, 8502−8511

Table 2. EXAFS Fitting Results, Top Number: Path Length R in Å, Below: σ^2 in 10^{-3} Å^2[a]

	BL25F		BL5F		BL5FZn20		BFY20	
	ox	red	ox	red	ox	red	ox	red
Fe—O	1.98	1.99	1.95	1.95	1.92	1.92	1.89	1.91
	9	18	11	9	10	8	7	7
M—O					1.97	1.97	2.27	2.28
					16	11	4	4
Fe—Ba	3.40	3.47	3.42	3.40	3.40	3.41	3.46	3.41
	2	8	4	13	11	10	10	11
M—Ba					3.42	3.41	3.56	3.57
					16	28	8	9
Fe—La	3.40	3.31						
	2	4						
Fe—Fe	3.96	3.93	3.90	3.85	3.72	3.78	3.71	3.78
	8	10	9	11	18	25	30	30
Fe—M					3.89	3.83	4.14	4.17
					3	24	7	7
Fe—Fe—O	3.96	3.96	3.90	3.88	3.78	3.81	3.74	3.79
	3	8	10	11	11	10	26	13
Fe—M—O					3.89	3.86	4.15	4.18
					5	15	5	7
Fe—O—Fe—O	3.96	3.99	3.90	3.90	3.83	3.85	3.77	3.81
	11	18	7	9	9	8	9	13
Fe—O—M—O					3.89	3.89	4.17	4.19
					2	15	9	9

	BSF		BSFZn20		SFZn20		SF
	ox	red	ox	red	ox	red	ox
Fe—O	1.97	1.93	1.91	1.92	1.92	1.95	1.95
	8	8	11	6	9	6	14
M—O			2.01	1.96	1.98	1.99	
			9	7	8	10	
Fe—Ba	3.38	3.39	3.35	3.32			
	2	3	2	4			
M—Ba			3.37	3.37			
			12	23			
Fe—Sr	3.38	3.39	3.36	3.33	3.35	3.31	3.31
	3	7	2	10	4	13	6
M—Sr			3.34	3.32	3.10	3.09	
			15	25	10	10	
Fe—Fe	3.94	3.83	3.74	3.76	3.84	3.91	3.88
	3	6	5	2	10	5	2
Fe—M			3.89	3.81	3.92	3.94	
			3	2	13	11	
Fe—Fe—O	3.94	3.84	3.78	3.80	3.84	3.91	3.89
	4	12	13	5	2	9	4
Fe—M—O			3.90	3.84	3.93	3.94	
			3	2	12	9	
Fe—O—Fe—O	3.94	3.85	3.83	3.84	3.84	3.91	3.91
	12	8	4	2	2	10	2
Fe—O—M—O			3.91	3.88	3.93	3.94	
			4	2	15	2	

[a]M = Zn,Y for doped samples (M—Fe is not separately indicated because it is constraint to equal Fe—M). The error on R is ±0.02 Å and around ±10% on σ^2.

leads to a distribution of B—A and B—B distances, owing to the different ionic radii of substitutional atoms. In the perovskite structure, the local environment of a B site cation in an ABO_3 perovskite is composed by: (a) first shell B—O, with six oxygen atoms; (b) second shell B—A, with eight cations. The A site may contain Ba, Sr, or La: they are fitted as separate subshells because of their different ion radii,[49] (c) third shell B—B, with six B atoms. For the doped samples, the third shell also contains the Fe—M distances, where M represents a Zn, Y dopant atom and is fitted as a separate subshell.

The distances and disorder factors were refined for each shell, while the coordination numbers were fixed according to the stoichiometry by taking the oxygen deficiency into account. In the fitting procedure, we assume a random oxygen vacancy distribution, which is supported by the fact that the investigated samples do not show any superstructure

https://dx.doi.org/10.1021/acs.chemmater.0c02655
Chem. Mater. 2020, 32, 8502−8511

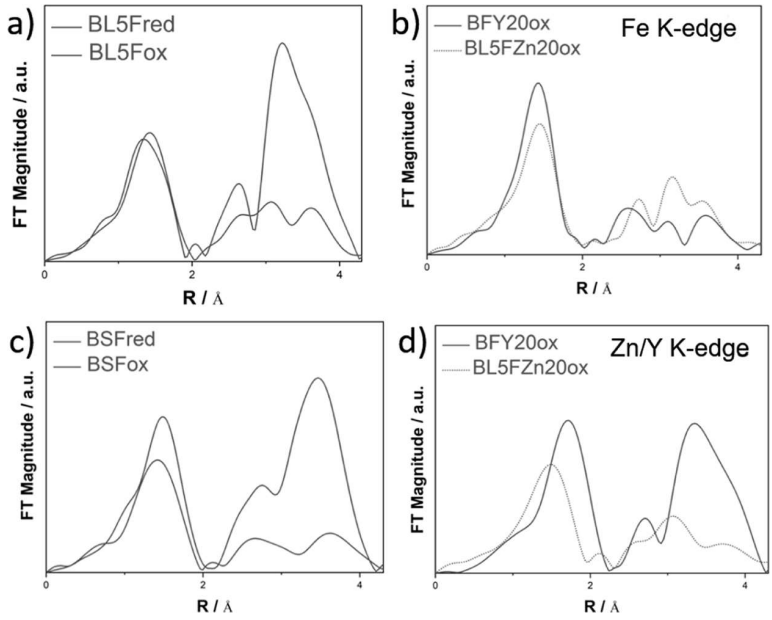

Figure 2. Fourier transform of EXAFS of representative samples (spectra of all samples are given in Supporting Information). (a–c) Fe K-edge, (d) Zn K-edge of BL5FZn20ox, and Y K-edge of BFY20ox.

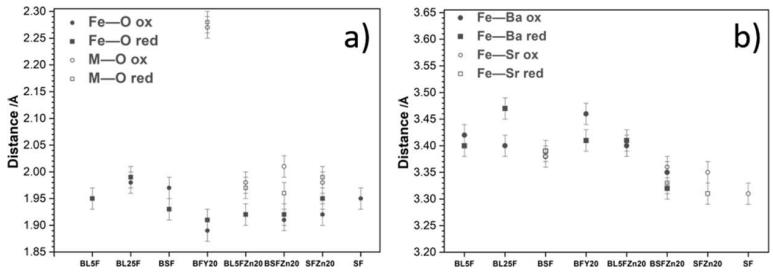

Figure 3. (a) Fe–O and M–O distances in oxidized (red symbols) and reduced (green) samples. (b) Fe–Ba and Fe–Sr distances in oxidized (red) and reduced (green) samples.

reflections caused by $V_o^{\bullet\bullet}$ ordering in XRD (reduced SF which acquires the brownmillerite structure is excluded from the EXAFS discussion). In the perovskite structure, multiple scattering effects are important because of many collinear arrangements of atoms: for this reason, to achieve a satisfactory fit, the distances B–O–B–O or B–O–B were also taken into account in the model.[50] In the perfect cubic perovskite structure, the B–O–B connection is linear, and the direct B–B distance equals the three-body multiple scattering path (MSP) B–O–B. In the case of B–O–B buckling, the angle is lower than 180°, and the direct distance is less than the MSP and the sum of the B–O bond lengths. For more fitting details, see Supporting Information. The results from the EXAFS analysis are reported in Table 2 and representative fits are shown in Figure 2.

3.2.1. Discussion: First and Second Shell. All samples show fairly similar first shell coordination, with a lower first-shell peak in the reduced samples. The Fe–O distances are in the range 1.89–1.98 Å in oxidized samples and 1.91–1.99 Å in reduced samples (Table 2, Figure 3a). This slight increase upon reduction is in agreement with the "chemical expansion" in the lattice parameters (Table 1), as also observed for other iron perovskites.[42,51] The Fe–O distances are not very sensitive to the presence of dopants on the A site (La^{3+},Sr^{2+}) or B site (Zn^{2+},Y^{3+}). The Zn–O and Y–O distances do not change much between oxidized and reduced samples. The Y–O bond length matches closely what is expected from its ionic radius (0.26 Å larger than Fe^{3+}). The large Y–O bond length is in part buffered by comparably short Fe–O distances in BFY20. On the contrary, the Zn–O bond length is shorter than that expected from the Zn^{2+} radius (0.1 Å larger than Fe^{3+}). The disorder is generally higher in reduced samples. The second shell distances are around 3.3–3.6 Å, without systematic variations between oxidized and reduced samples (Figure 3b).

3.2.2. Discussion: Third Shell. The most pronounced differences between the various compositions and also between their oxidized and reduced forms are seen in the third shell (Fe–Fe and Fe–M distances). This is evident already in the Fourier transforms in Figure 2. Several samples exhibit a very pronounced third-shell peak, indicating significant long-range order, for example, oxidized BL5F, BSF, and BL25F. On the contrary, the third shell peak is strongly depressed by (i) reduction treatment, inducing a large $V_o^{\bullet\bullet}$ concentration (Figure 2a,c) and (ii) Zn or Y doping on the B-site of oxidized samples (Figure 2b,d). The intensity of the third-shell peak has significant contributions from MSPs, which are most important for collinear B–O–B configurations.[22] Nonlinear

https://dx.doi.org/10.1021/acs.chemmater.0c02655
Chem. Mater. 2020, 32, 8502–8511

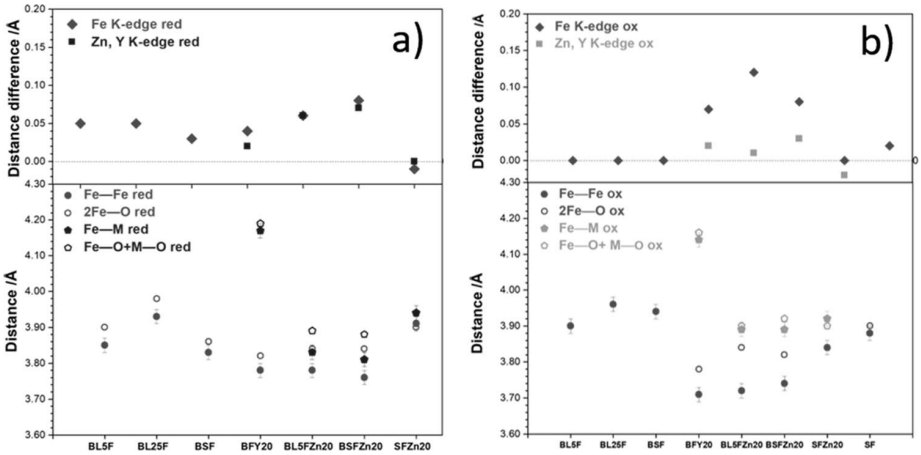

Figure 4. Bottom plots: Fe−Fe, Fe−M direct distances (solid symbols) compared to 2·Fe−O and Fe−O + M−O (open symbols), respectively. Top: Difference between Fe−Fe and 2·Fe−O (diamonds), and Fe−M and Fe−O + M−O (squares). (a) Reduced samples and (b) oxidized samples.

B−O−B configurations represent local distortions relative to the average cubic structure. Such distortions can arise from a high oxygen vacancy concentration (the reduced samples have around 0.5 oxygen vacancies per ABO_3 formula unit). They can also be caused by substitution on the B-site by cations with different sizes such as Zn^{2+} or Y^{3+}. In comparison, the substitution of Ba^{2+} by the smaller Sr^{2+} on the A-site appears not to have much effect (compare oxidized BL5F and BSF in Figure 2a,c). The overall disorder in the third-shell distances (σ^2 for Fe−Fe, Fe−M, and MSP) is higher for the reduced samples compared to the oxidized ones. Also, it increases drastically upon partial substitution of Fe by the oversized Zn or Y ions, approaching 0.03 $Å^2$ in some cases. At such a high level of static disorder, these third shell features are almost completely washed out in the Fourier transform plots. These tendencies correlate well with the deviation of B−O−B configurations from linearity as discussed below.

Inspection of the fitted Fe−Fe distance in Table 2 shows that in some cases, the direct cation−cation distance is less than twice the Fe−O distance. This phenomenon also results in the MSP involving noncollinear Fe−O−Fe configurations, being longer than Fe−Fe. In Figure 4, the effect of the buckling of the Fe−O−Fe configurations is plotted for different samples, comparing the direct Fe−Fe distances with the paths involving oxygen as a measure of local deviation from collinearity. The paths involving O comprise the single scattering Fe−O distance, as well as Fe−Fe−O and Fe−O−Fe−O MSP (these MSPs are coupled to Fe−O by constraints; see Supporting Information). Similar considerations hold for Fe−M distances compared with the sum of Fe−O and M−O and the respective MSP. Figure 4a,b (top) presents the differences between 2·Fe−O or Fe−O + M−O and the direct Fe−Fe, Fe−M distances (a difference of 0.1 Å corresponds to a buckling angle of about 154°). Qualitatively, the trends concerning buckling can also be recognized in the Fourier transforms in Figure 2 and Supporting Information, which confirms the robustness of the analysis.

Reduced samples (Figure 4a) exhibit a significant Fe−O−Fe buckling even in the absence of B-site dopants, apparently related to the high oxygen vacancy concentration (0.37−0.67 $V_o^{\bullet\bullet}$ per formula unit). An analysis of the geometries of $BaFeO_{3-\delta}$ supercells from DFT calculations by Hoedl et al.[18] shows that the oxygen vacancy leads to two effects: (i) the two B site cations move farther apart and (ii) four oxygen ions attached to each of these B cations are pulled toward the vacancy. These two effects lead to a significant buckling of the Fe−O−Fe in oxygen-deficient $BaFeO_{3-\delta}$. For δ up to 0.25, the Fe−O−Fe close to a $V_o^{\bullet\bullet}$ displays moderate buckling with an angle of around 170°, while for larger δ values, a broader distribution of buckling angles from 157 to 176° is found. This is in good agreement with the EXAFS results in Figure 4a. The buckling of the reduced BFY20 is comparable to reduced BL5F, BSF; the one of Zn-doped BL5FZn20 and BSFZn20 is larger.

For the oxidized samples without Zn or Y, the difference between Fe−Fe and 2·Fe−O is low (Figure 4b, top), which suggests a linear Fe−O−Fe arrangement, reflecting an ideal cubic perovskite structure. The above defined difference increases significantly for oxidized BFY20, BL5FZn20, and BSFZn20, indicating bent Fe−O−Fe configurations instead: because in bent configurations, the so-called focusing effect of the collinear configurations is lost; this also explains the lower intensity of the third-shell peak in the Fourier transforms in Figure 2. Zn,Y-doped samples contain 0.1−0.2 $V_o^{\bullet\bullet}$ per formula unit even when all iron is in the formal 4+ oxidation state (Table 1). However, comparing the doped samples to the reduced BL5F, BL25F, and BSF samples which have 0.38−0.5 $V_o^{\bullet\bullet}$ per formula unit but less buckling (only 0.05−0.1 Å, Figure 4a), it is clear that the strong buckling in these oxidized doped samples cannot be attributed to the $V_o^{\bullet\bullet}$ alone, but it is also caused by the presence of oversized dopants in the B-site. According to the analysis of the respective Y and Zn edges, the Fe−O−M configurations are less distorted than Fe−O−Fe (orange symbols in Figure 4b).

DFT calculations of $Ba_8Fe_7ZnO_{23}$ and $Ba_8Fe_6Y_2O_{23}$ supercells can help to interpret this observation (more details described in Supporting Information). The composition of supercells is close to that of oxidized BL5FZn20 and BFY20 samples with iron in the formal 4+ oxidation state. A typical configuration of a $V_o^{\bullet\bullet}$ located between a Fe^{4+} and a Zn^{2+} is shown in Figure S11. The distance between these Fe^{4+} and Zn^{2+} is increased relative to the pseudocubic lattice parameter, which corresponds to an outward displacement of both cations. The exact distortion pattern depends on the

https://dx.doi.org/10.1021/acs.chemmater.0c02655
Chem. Mater. 2020, 32, 8502−8511

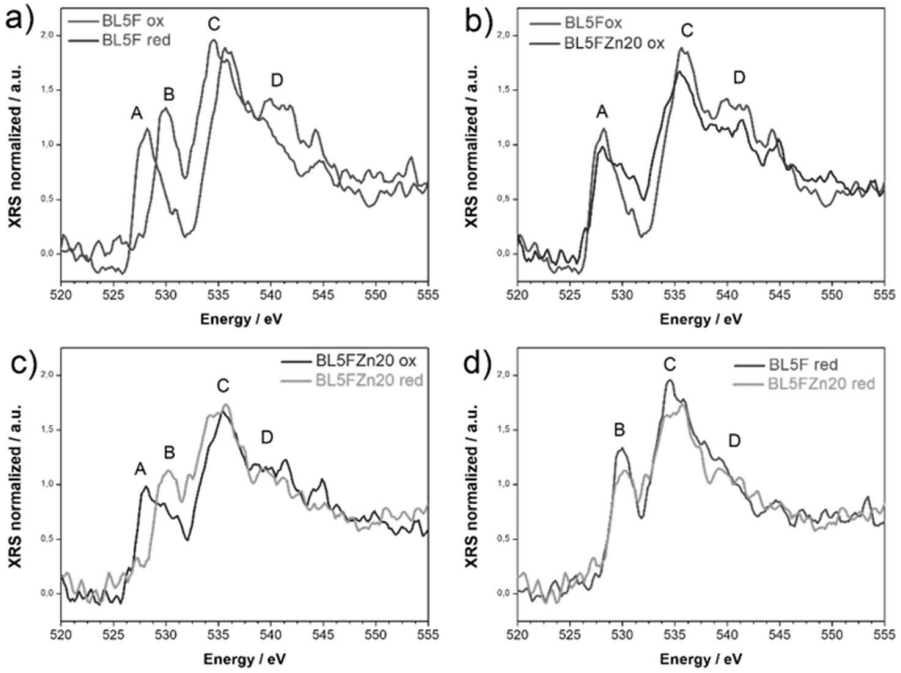

Figure 5. O K-edge X-ray absorption spectra (XRS); the spectra are smoothed by five-point averaging. (a) Oxidized and reduced BL5F, (b) oxidized BL5F and BL5FZn, (c) oxidized and reduced BL5FZn20, (d) reduced BL5F and BL5FZn.

configuration of the $V_o^{\bullet\bullet}$ relative to the $Y^{3+}$and Zn^{2+} dopants (values given in Table S2 and plotted in Figure S12a). For both $Ba_8Fe_6Y_2O_{23}$ and $Ba_8Fe_7ZnO_{23}$, the average displacement is larger than in an undoped $Ba_8Fe_8O_{23}$ supercell (which corresponds to a partially reduced sample), with the larger average displacement for the Zn-doped material. Such an outward cation displacement then leads to a buckling of the respective (Fe,M)−O−Fe configurations. Figure S12b shows that buckling is weaker for M−O−Fe than for Fe−O−Fe, which agrees well with Figure 4b. Interestingly, the calculated outward Fe,Zn displacements in $Sr_8Fe_8O_{23}$ and $Sr_8Fe_7ZnO_{23}$ supercells are smaller compared to the barium ferrate supercells. Two factors may contribute to that (i) $SrFeO_3$ has a stiffer lattice than $BaFeO_3$,[52] which is expected to generally disfavor ion displacements and (ii) outward displacement of a B cation close to a $V_o^{\bullet\bullet}$ is smaller when the B-site dopant is strongly oversized owing to the lack of available space (Zn^{2+} is relatively more oversized than Fe in $SrFeO_3$ than in $BaFeO_3$). This decreased cation displacement agrees well with the low buckling in SFox and SFZn20ox (Figure 4b).

In conclusion, the combination of $V_o^{\bullet\bullet}$ with B-site acceptor dopants—but avoiding too much size mismatch—appears most effective to bend the Fe−O−Fe, Fe−O−M configurations. For perovskites, it is well known that the width of the electronic band formed by the cations' d- and oxygen p-orbitals decreases strongly when the B−O−B configuration is bent (e.g., in rare-earth nickelates, buckling suppresses the metallic charge transport, and in mixed-valent manganates, buckling preserves charge ordering to higher temperatures[30−32]). The consequences of the strong B−O−B buckling in Zn,Y-doped perovskites for the proton incorporation will be further discussed in Section 3.4.

3.3. Oxygen XRS. In the present publication, we focus on a phenomenological analysis of the oxygen XRS spectra of oxidized and reduced BL5F and BL5FZn20, which allows us to recognize their characteristic changes and relate them to XANES and EXAFS results. The extended quantitative XRS analysis applying specific quantum-chemical calculations (comprising further $BaFeO_{3-\delta}$-related perovskites and $BaZrO_3$ as redox-inactive reference material) will be reported separately. The oxygen K-edge spectra are reported in Figure 5. These excitations correspond to electronic transitions from the O 1s core level to 2p states, which are hybridized with the orbitals of the transition metal (Fe,Zn), thereby reflecting the extent of covalence of the (Fe,Zn)−O bonds.[29] The peaks can be assigned as follows: the first double feature in the pre-edge region between 525 and 530 eV (peaks A and B in Figure 5) is attributed to unoccupied states of TM 3d−O 2p mixed character generated by the hybridization of TM 3d and O 2p in the octahedral crystal field (TM = Fe, Zn). This forms e_g and t_{2g} molecular orbitals (not fully experimentally resolved), which correspond to σ- and π-type TM−O interactions. Peak C at 535−537 eV corresponds to bands derived from Ba/La 5d states. Finally, the broader peak D at 540 eV is due to bands of the mixed O 2p and (Fe,Zn)4s and 4p character.[53]

The comparison of the oxidized with the respective reduced samples highlights a shift of peak positions and/or modification of their intensity. The changes in the XRS spectra (Figure 5a,c) clearly demonstrate that the oxygen electronic states are severely modified by the oxidation process. These changes are at least as pronounced as those for iron, to which the valence change is formally assigned (3+ ↔ 4+). These changes are especially evident for BL5F: the pre-edge peak at 528 eV (A) is converted into a peak at 530 eV (B), and peak C shifts by 1.5 eV. The pre-edge peak (A → B) and peak C both shift, although to a smaller degree than for BL5F. The hole formation because of oxidation in these samples is represented by the defect chemical reaction

$$\frac{1}{2}O_2 + V_o^{\bullet\bullet} \rightarrow O_o^{\times} + 2h^{\bullet}$$

https://dx.doi.org/10.1021/acs.chemmater.0c02655
Chem. Mater. 2020, 32, 8502−8511

The changes observed in O K-edge spectra clearly show that in the oxidation process of these samples, both iron (formally Fe^{3+} to Fe^{4+}) and oxygen (formally O^{2-} to O^{-}) are involved to a significant extent. These changes are mainly observed in the pre-edge peaks. However, according to literature, these variations cannot be explained in terms of population and depopulation of the e_g and t_{2g} states, but rather by a concerted effect which involves both the O 2p/TM 3d orbital population and their degree of covalency[54] (a more detailed analysis will be provided in a dedicated paper).

Considering the oxidized samples shown in Figure 5b, it can be recognized that the pre-edge peak A is more pronounced for BL5F than for BL5FZn20 and also shows a stronger change in comparison to the reduced sample. This may be attributed to a larger share of holes located in oxygen states. Figure 5d shows that for the reduced samples the XRS spectra of BL5F and BL5FZn20 are more similar, regarding the positions and widths of peaks B and C. This can be rationalized by the fact that both reduced samples are distorted owing to the presence of oxygen vacancies. The relation between geometrical distortions and modifications in the electronic structure will be further discussed in the next section.

3.4. Concluding Discussion. We can summarize the results of the different techniques as follows:

(i) Fe K-edge XANES: Comparing reduced and oxidized samples, the edge shift is larger for SF and SFZn20, intermediate for BL5F, and weakest for BFY20 and BL5FZn20; this indicates that in the Sr-rich perovskites, the iron is closer to the formal 4+ oxidation state. The partial replacement of iron in the B-site by Y^{3+}/Zn^{2+}, which are larger and less charged, may leave more electron density at the oxide ions: therefore, in BFY20 and BL5FZn20, iron is closer to the formal 3+ oxidation state, even for fully oxidized samples, compared to BL5F.

(ii) EXAFS: Oxidized samples without Zn,Y show very small deviation from a local cubic perovskite ordering, which is evident from the very strong third shell peak in the Fourier transforms. The partial substitution of Fe by Y^{3+}, and even more Zn^{2+}, in Ba-containing perovskites leads to a strong suppression of the third shell peak that is due to significant static disorder and buckling of B−O−B connections. The rather smaller B−O−B buckling in SFZn20ox is most probably related to the higher stiffness of the lattice. The reduced samples are all very heavily disordered on the local scale because of their high oxygen vacancy concentration.

(iii) O K-edge XRS: As it was already observed in the case of the Fe K-edge XANES, the different samples show more similarities in their reduced state: for both BL5F and BL5FZn20, the oxidation reaction strongly affects both the O K-edge and Fe K-edge spectra, giving direct experimental indication for a significant degree of charge transfer and related covalency in the Fe−O bonds (a full analysis of the DFT density of states of $BaFeO_3$ and related materials will be reported separately). The changes are more pronounced for BL5F, which might be related to the absence of oversized B cations: in this case, the corresponding B−O−B buckling—evidenced by EXAFS—tends to decrease Fe and O orbital overlap.[30−32]

These findings can then also be compared to the results of proton uptake measurements for reduced samples, which amounts to 5−10 mol % for BFY20 and BL5FZn20, 2−3 mol % for BSF and BL5F, and drops to 0.6 mol % for SFZn20 and <0.2 mol % for SF (measured at 250 °C in 17 mbar H_2O).[10] The dissociative water incorporation comprises protonation of a regular oxide ion and filling of a $V_o^{\bullet\bullet}$ by a hydroxide ion. Thus, it is not surprising to see that this reaction is most favorable for the $(Ba,Sr,La)(Fe,Zn,Y)O_{3-\delta}$ perovskites that combine a high content of Ba (as the most basic A site cation of this materials family) with the partial Fe substitution by Y,Zn. The latter has a two-fold effect: it replaces some Fe with are larger and less-charged Y,Zn cations (increasing the basic character of the material), and the induced B−O−B buckling decreases the Fe−O covalency and thus delocalization of holes from formal Fe^{4+} to O (which decreases the basicity of the oxide ions). These relations and the consequence for proton uptake are schematically depicted in Figure 6.

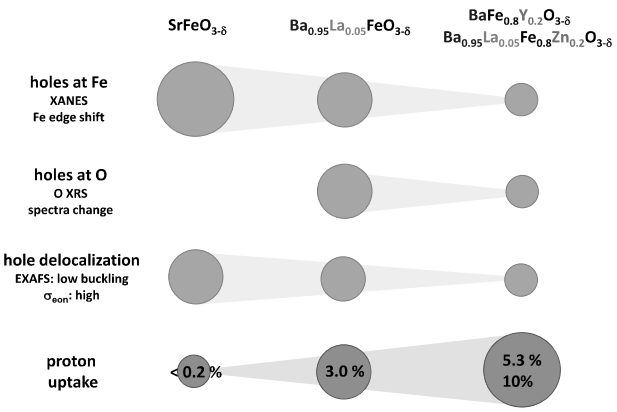

Figure 6. Schematic summary of trends in electronic and geometrical structures of $(Ba,Sr,La)(Fe,Zn,Y)O_{3-\delta}$ perovskites, the size of the circles indicates the strength of the effect. The degree of hole delocalization is concluded from EXAFS results (large Fe−O−Fe/M buckling leads to low delocalization) and electronic conductivity (σ_{eon} in O_2 at 600 °C, decreasing from 100 S/cm for SF[55] to 10 S/cm for BL5F and ≈1 S/cm for BFY20[10]). The corresponding proton uptake at 250 °C is taken from Zohourian et al.[10]

4. CONCLUSIONS

The present investigation of $(Ba,Sr,La)(Fe,Zn,Y)O_{3-\delta}$ perovskites reveals a complex interplay of cation composition, structural distortions, and features in the electronic structure, which together affect the proton uptake desired for an application as cathode materials in protonic ceramic cells. The strongest buckling of interoctahedral Fe−O−Fe(M) bonds is observed when oxygen vacancies and moderately oversized B-site dopants such as Zn^{2+} are present. The less-pronounced distortions in the $SrFe_{0.8}Zn_{0.2}O_{3-\delta}$ perovskite are related to the higher stiffness of the Ba-free structure. The oxygen states are very sensitive to the covalency of the Fe−O bonds and charge transfer to the transition metal cations, and this, in turn, affects the oxide ions' basicity. The least effective hole transfer to oxygen is found for the most distorted materials, which in turn exhibit the highest proton uptake. Providing an overall consistent picture of the interplay of chemical, geometrical, and electronic structure features and how they affect the proton uptake, these insights can serve as guidelines for further PCFC cathode material optimization.

https://dx.doi.org/10.1021/acs.chemmater.0c02655
Chem. Mater. 2020, 32, 8502−8511

■ ASSOCIATED CONTENT

Supporting Information

The Supporting Information is available free of charge at https://pubs.acs.org/doi/10.1021/acs.chemmater.0c02655.

XRD, XANES edge energies, EXAFS path scheme and fitting constraints, plots of the Fourier transforms, DFT computational details, and results (PDF)

■ AUTHOR INFORMATION

Corresponding Authors

Francesco Giannici − *Dipartimento di Fisica e Chimica, Università degli Studi di Palermo, Palermo 90128, Italy;* orcid.org/0000-0003-3086-956X; Email: francesco.giannici@unipa.it

Alessandro Longo − *European Synchrotron Radiation Faciliy, Grenoble 38000, France; Istituto per lo Studio dei Materiali Nanostrutturati (ISMN)-CNR, UOS Palermo, Palermo 00185, Italy;* orcid.org/0000-0002-8819-2128; Email: alessandro.longo@cnr.it

Rotraut Merkle − *Max Planck Institute for Solid State Research, Stuttgart 70569, Germany;* orcid.org/0000-0003-3811-8963; Email: r.merkle@fkf.mpg.de

Authors

Giulia Raimondi − *Max Planck Institute for Solid State Research, Stuttgart 70569, Germany;* orcid.org/0000-0002-1425-4242

Alessandro Chiara − *Dipartimento di Fisica e Chimica, Università degli Studi di Palermo, Palermo 90128, Italy*

Maximilian F. Hoedl − *Max Planck Institute for Solid State Research, Stuttgart 70569, Germany;* orcid.org/0000-0003-3166-6772

Antonino Martorana − *Dipartimento di Fisica e Chimica, Università degli Studi di Palermo, Palermo 90128, Italy;* orcid.org/0000-0003-1911-1627

Joachim Maier − *Max Planck Institute for Solid State Research, Stuttgart 70569, Germany;* orcid.org/0000-0003-2274-6068

Complete contact information is available at: https://pubs.acs.org/10.1021/acs.chemmater.0c02655

Notes

The authors declare no competing financial interest.

■ ACKNOWLEDGMENTS

We thank Helga Hoier (MPI for Solid State Research, Stuttgart) for XRD, Samir Hammou (MPI for Intelligent Systems, Stuttgart) for ICP-OES, Christoph Sahle (ESRF, Grenoble) for the insights on XRS data reduction, and Chiara Cavallari (ESRF, Grenoble) for support at the beamline ID20.

■ REFERENCES

(1) Kreuer, K. D. Proton-conducting oxides. *Ann. Rev. Mater. Res.* **2003**, *33*, 333−359.

(2) Duan, C.; Tong, J.; Shang, M.; Nikodemski, S.; Sanders, M.; Ricote, S.; Almansoori, A.; OHayre, R. Readily processed protonic ceramic fuel cells with high performance at low temperatures. *Science* **2015**, *349*, 1321−1326.

(3) Bae, K.; Jang, D. Y.; Choi, H. J.; Kim, D.; Hong, J.; Kim, B. K.; Lee, J.-H.; Son, J.-W.; Shim, J. H. Demonstrating the potential of yttrium-doped barium zirconate electrolyte for high-performance fuel cells. *Nat. Commun.* **2017**, *8*, 14553.

(4) Choi, S.; Kucharczyk, C. J.; Liang, Y.; Zhang, X.; Takeuchi, I.; Ji, H.-I.; Haile, S. M. Exceptional power density and stability at intermediate temperatures in protonic ceramic fuel cells. *Nat. Energy* **2018**, *3*, 202.

(5) An, H.; Lee, H.-W.; Kim, B.-K.; Son, J.-W.; Yoon, K. J.; Kim, H.; Shin, D.; Ji, H.-I.; Lee, J.-H. A 5×5 cm^2 protonic ceramic fuel cell with a power density of 1.3 W cm^{-2} at 600 °C. *Nat. Energy* **2018**, *3*, 870−875.

(6) Duan, C.; Huang, J.; Sullivan, N.; O'Hayre, R. Proton-conducting oxides for energy conversion and storage. *Appl. Phys. Rev.* **2020**, *7*, 011314.

(7) Merkle, R.; Poetzsch, D.; Maier, J. Oxygen reduction reaction at cathodes on proton conducting oxide electrolytes: contribution from three phase boundary compared to bulk path. *ECS Trans.* **2015**, *66*, 95−102.

(8) Strandbakke, R.; Cherepanov, V. A.; Zuev, A. Y.; Tsvetkov, D. S.; Argirusis, C.; Sourkouni, G.; Prünte, S.; Norby, T. Gd-and Pr-based double perovskite cobaltites as oxygen electrodes for proton ceramic fuel cells and electrolyser cells. *Solid State Ionics* **2015**, *278*, 120−132.

(9) Wang, Z.; Yang, W.; Shafi, S. P.; Bi, L.; Wang, Z.; Peng, R.; Xia, C.; Liu, W.; Lu, Y. A high performance cathode for proton conducting solid oxide fuel cells. *J. Mater. Chem. A* **2015**, *3*, 8405−8412.

(10) Zohourian, R.; Merkle, R.; Raimondi, G.; Maier, J. Mixed-Conducting Perovskites as Cathode Materials for Protonic Ceramic Fuel Cells: Understanding the Trends in Proton Uptake. *Adv. Funct. Mater.* **2018**, *28*, 1801241.

(11) Grimaud, A.; Mauvy, F.; Bassat, J. M.; Fourcade, S.; Rocheron, L.; Marrony, M.; Grenier, J. C. Hydration Properties and Rate Determining Steps of the Oxygen Reduction Reaction of Perovskite-Related Oxides as H+-SOFC Cathodes. *J. Electrochem. Soc.* **2012**, *159*, B683−B694.

(12) Han, D.; Okumura, Y.; Nose, Y.; Uda, T. Synthesis of $La_{1-x}Sr_xSc_{1-y}Fe_yO_{3-\delta}$ (LSSF) and measurement of water content in LSSF, LSCF and LSC hydrated in wet artificial air at 300 °C. *Solid State Ionics* **2010**, *181*, 1601−1606.

(13) Hashimoto, D.; Han, D.; Uda, T. Dependence of lattice constant of Ba, Co-contained perovskite oxides on atmosphere, and measurements of water content. *Solid State Ionics* **2014**, *262*, 687−690.

(14) Vøllestad, E.; Schrade, M.; Segalini, J.; Strandbakke, R.; Norby, T. Relating defect chemistry and electronic transport in the double perovskite $Ba_{1-x}Gd_{0.8}La_{0.2+x}Co_2O_{6-\delta}$ (BGLC). *J. Mater. Chem. A* **2017**, *5*, 15743−15751.

(15) Poetzsch, D.; Merkle, R.; Maier, J. Proton conductivity in mixed-conducting BSFZ perovskite from thermogravimetric relaxation. *Phys. Chem. Chem. Phys.* **2014**, *16*, 16446.

(16) Zohourian, R.; Merkle, R.; Maier, J. Proton uptake into the protonic cathode material $BaCo_{0.4}Fe_{0.4}Zr_{0.2}O_{3-\delta}$ and comparison to protonic electrolyte materials. *Solid State Ionics* **2017**, *299*, 64−69.

(17) Poetzsch, D.; Merkle, R.; Maier, J. Proton uptake in the H^+-SOFC cathode material $Ba_{0.5}Sr_{0.5}Fe_{0.8}Zn_{0.2}O_{3-\delta}$: transition from hydration to hydrogenation with increasing oxygen partial pressure. *Faraday Discuss.* **2015**, *182*, 129−143.

(18) Hoedl, M. F.; Gryaznov, D.; Merkle, R.; Kotomin, E. A.; Maier, J. Interdependence of Oxygenation and Hydration in Mixed-Conducting $(Ba,Sr)FeO_{3-\delta}$ Perovskites Studied by Density Functional Theory. *J. Phys. Chem. C* **2020**, *124*, 11780−11789.

(19) Longo, A.; Giannici, F.; Balerna, A.; Ingrao, C.; Deganello, F.; Martorana, A. Local environment of yttrium in Y-doped barium cerate compounds. *Chem. Mater.* **2006**, *18*, 5782−5788.

(20) Giannici, F.; Longo, A.; Deganello, F.; Balerna, A.; Arico, A.; Martorana, A. Local environment of Barium, Cerium and Yttrium in $BaCe_{1-x}Y_xO_{3-\delta}$ ceramic protonic conductors. *Solid State Ionics* **2007**, *178*, 587−591.

(21) Giannici, F.; Longo, A.; Balerna, A.; Kreuer, K.-D.; Martorana, A. Proton dynamics in In:$BaZrO_3$: Insights on the atomic and electronic structure from X-ray absorption spectroscopy. *Chem. Mater.* **2009**, *21*, 2641−2649.

(22) Giannici, F.; Shirpour, M.; Longo, A.; Martorana, A.; Merkle, R.; Maier, J. Long-Range and Short-Range Structure of Proton-Conducting Y:$BaZrO_3$. *Chem. Mater.* **2011**, *23*, 2994−3002.
(23) Wang, N.; Hinokuma, S.; Ina, T.; Toriumi, H.; Katayama, M.; Inada, Y.; Zhu, C.; Habazaki, H.; Aoki, Y. Incorporation of bulk proton carriers in cubic perovskite manganite driven by interplays of oxygen and manganese redox. *Chem. Mater.* **2019**, *31*, 8383−8393.
(24) Joly, Y. X-ray absorption near-edge structure calculations beyond the muffin-tin approximation. *Phys. Rev. B* **2001**, *63*, 125120.
(25) Joly, Y.; Cavallari, C.; Guda, S. A.; Sahle, C. J. Full-Potential Simulation of X-ray Raman Scattering Spectroscopy. *J. Chem. Theory Comput.* **2017**, *13*, 2172−2177.
(26) Fehse, M.; Sahle, C. J.; Hogan, M. P.; Cavallari, C.; Kelder, E. M.; Alfredsson, M.; Longo, A. Bulk-Sensitive Soft X-ray Edge Probing for Elucidation of Charge Compensation in Battery Electrodes. *J. Phys. Chem. C* **2019**, *123*, 24396−24403.
(27) Longo, A.; Theofanidis, S. A.; Cavallari, C.; Srinath, N. V.; Hu, J.; Poelman, H.; Sabbe, M. K.; Sahle, C. J.; Marin, G. B.; Galvita, V. V. What makes Fe-modified $MgAl_2O_4$ an active catalyst support? Insight from X-ray Raman Scattering. *ACS Catal.* **2020**, *10*, 6613−6622.
(28) Frati, F.; Hunault, M. O. J. Y.; de Groot, F. M. F. Oxygen K-edge X-ray Absorption Spectra. *Chem. Rev.* **2020**, *120*, 4056−4110.
(29) Longo, A.; Liotta, L. F.; Banerjee, D.; La Parola, V.; Puleo, F.; Cavallari, C.; Sahle, C. J.; Moretti Sala, M.; Martorana, A. The Effect of Ni Doping on the Performance and Electronic Structure of LSCF Cathodes Used for IT-SOFCs. *J. Phys. Chem. C* **2018**, *122*, 1003−1013.
(30) Medarde, M.; Mesot, J.; Lacorre, P.; Rosenkranz, S.; Fischer, P.; Gobrecht, K. High-pressure neutron-diffraction study of the metallization process in $PrNiO_3$. *Phys. Rev. B* **1995**, *52*, 9248.
(31) Radaelli, P. G.; Iannone, G.; Marezio, M.; Hwang, H. Y.; Cheong, S.-W.; Jorgensen, J. D.; Argyriou, D. N. Structural effects on the magnetic and transport properties of perovskite $A_{1-x}A_x'MnO_3$ (x=0.25, 0.30). *Phys. Rev. B* **1997**, *56*, 8265.
(32) Salamon, M. B.; Jaime, M. The physics of manganite: Structure and transport. *Rev. Mod. Phys.* **2001**, *73*, 583−628.
(33) Shang, M.; Tong, J.; O'Hayre, R. A promising cathode for intermediate temperature protonic ceramic fuel cells: $BaCo_{0.4}Fe_{0.4}Zr_{0.2}O_{3-\delta}$. *RSC Adv.* **2013**, *36*, 15769−15775.
(34) Dong, F.; Chen, D.; Chen, Y.; Zhao, Q.; Shao, Z. La-doped $BaFeO_{3-\delta}$ perovskite as a cobalt-free oxygen reduction electrode for solid oxide fuel cells with oxygen-ion conducting electrolyte. *J. Mater. Chem.* **2012**, *22*, 15071−15079.
(35) Chen, C.; Chen, D.; Gao, Y.; Shao, Z.; Ciucci, F. Computational and experimental analysis of $Ba_{0.95}La_{0.05}FeO_{3-\delta}$ as a cathode material for solid oxide fuel cells. *J. Mater. Chem. A* **2014**, *2*, 14154−14163.
(36) Mizusaki, J.; Yoshihiro, M.; Yamauchi, S.; Fueki, K. Non-stoichiomentry and defect structure of the perovskite-type oxides $La_{1-x}Sr_xFeO_{3-\delta}$. *J. Solid State Chem.* **1985**, *58*, 257−266.
(37) Mizusaki, J.; Okayasu, M.; Yamauchi, S.; Fueki, K. Non-stoichiomentry and phase relationship of the $SrFeO_{2.5}$- $SrFeO_3$ system at high temperature. *J. Solid State Chem.* **1992**, *99*, 166−172.
(38) Klementev, K. V. Package VIPER (visual processing in EXAFS researches) for windows. *Nucl. Instrum. Methods Phys. Res., Sect. A* **2000**, *448*, 299−301.
(39) Rehr, J. J.; Albers, R. C. Theoretical Approaches to X-ray Absorption Fine Structure. *Rev. Mod. Phys.* **2000**, *72*, 621−654.
(40) Huotari, S.; Sahle, C. J.; Henriquet, C.; Al-Zein, A.; Martel, K.; Simonelli, L.; Verbeni, R.; Gonzalez, H.; Lagier, M.-C.; Ponchut, C.; Moretti Sala, M.; Krisch, M.; Monaco, G. A large-solid-angle X-ray Raman scattering spectrometer at ID20 of the European Synchrotron Radiation Facility. *J. Synchrotron Radiat.* **2017**, *24*, 521−530.
(41) Sahle, C. J.; Mirone, A.; Niskanen, J.; Inkinen, J.; Krisch, M.; Huotari, S. Planning, performing and analyzing X-ray Raman scattering experiments. *J. Synchrotron Radiat.* **2015**, *22*, 400−409.
(42) Vračar, M.; Kuzmin, A.; Merkle, R.; Purans, J.; Kotomin, E. A.; Maier, J.; Mathon, O. Jahn-Teller distortion around Fe^{4+} in $Sr(Fe_xTi_{1-x})O_{3-\delta}$ from X-ray absorption spectroscopy, X-ray diffraction, and vibrational spectroscopy. *Phys. Rev. B* **2007**, *76*, 174107.
(43) Mueller, D. N.; De Souza, R. A.; Brendt, J.; Samuelis, D.; Martin, M. Oxidation states of the transition metal cations in the highly nonstoichiometric perovskite-type oxide $Ba_{0.1}Sr_{0.9}Co_{0.8}Fe_{0.2}O_{3-\delta}$. *J. Mater. Chem.* **2009**, *19*, 1960−1963.
(44) Wilke, M.; Farges, F.; Petit, P.-E.; Brown, G. E.; Martin, F. Oxidation state and coordination of Fe in minerals: An Fe K-XANES spectroscopic study. *Am. Mineral.* **2001**, *86*, 714−730.
(45) Itoh, T.; Shirasaki, S.; Ofuchi, H.; Hirayama, S.; Honma, T.; Nakayama, M. Oxygen partial pressure dependence of in-situ X-ray absorption spectroscopy at the Co and Fe K edges for $(La_{0.6}Sr_{0.4})(Co_{0.2}Fe_{0.8})O_{3-\delta}$. *Solid State Commun.* **2012**, *152*, 278−283.
(46) Woolley, R. J.; Illy, B. N.; Ryan, M. P.; Skinner, S. J. In situ determination of the nickel oxidation state in $La_2NiO_{4+\delta}$ and $La_4Ni_3O_{10-\delta}$ using X-ray absorption near-edge structure. *J. Mater. Chem.* **2011**, *21*, 18592−18596.
(47) Kim, D.-Y.; Miyoshi, S.; Tsuchiya, T.; Yamaguchi, S. Electronic defect formation in Fe-doped $BaZrO_3$ studied by X-ray absorption spectroscopy. *Chem. Mater.* **2014**, *26*, 927−934.
(48) Hong, W. T.; Stoerzinger, K. A.; Lee, Y.-L.; Giordano, L.; Grimaud, A.; Johnson, A. M.; Hwang, J.; Crumlin, E. J.; Yang, W.; Shao-Horn, Y. Charge-transfer-energy-dependent oxygen evolution reaction mechanisms for perovskite oxides. *Energy Environ. Sci.* **2017**, *10*, 2190−2200.
(49) Shannon, R. D. Revised Effective Ionic Radii and Systematic Studies of Interatomic Distances in Halides and Chalcogenides. *Acta Crystallogr., Sect. A: Cryst. Phys., Diffr., Theor. Gen. Crystallogr.* **1976**, *32*, 751−767.
(50) Giannici, F.; Gregori, G.; Aliotta, C.; Longo, A.; Maier, J.; Martorana, A. Structure and oxide ion conductivity: local order, defect interactions and grain boundary effects in acceptor-doped ceria. *Chem. Mater.* **2014**, *26*, 5994−6006.
(51) Lein, H.; Wiik, K.; Grande, T. Thermal and chemical expansion of mixed conducting $La_{0.5}Sr_{0.5}Fe_{1-x}Co_xO_{3-\delta}$ materials. *Solid State Ionics* **2006**, *177*, 1795−1798.
(52) The Materials Project. Bulk and Shear Moduli Calculated by Density Functional Theory. https://materialsproject.org (accessed May 2020).
(53) Benfatto, M.; Joly, Y.; Natoli, C. R. Critical reexamination of the experimental evidence of orbital ordering in $LaMnO_3$ and $La_{0.5}Sr_{1.5}MnO_4$. *Phys. Rev. Lett.* **1999**, *83*, 636−639.
(54) Mueller, D. N.; Machala, M. L.; Bluhm, H.; Chueh, W. C. Redox activity of surface oxygen anions in oxygen-deficient perovskite oxides during electrochemical reactions. *Nat. Commun.* **2014**, *6*, 6097.
(55) Hombo, J.; Matsumoto, Y.; Kawano, T. Electrical conductivities of $SrFeO_{3-\delta}$ and $BaFeO_{3-\delta}$ perovskites. *J. Solid State Chem.* **1990**, *84*, 138−143.

https://dx.doi.org/10.1021/acs.chemmater.0c02655
Chem. Mater. 2020, 32, 8502−8511